JAAS

Accepted Manuscript

This is an *Accepted Manuscript*, which has been through the Royal Society of Chemistry peer review process and has been accepted for publication.

Accepted Manuscripts are published online shortly after acceptance, before technical editing, formatting and proof reading. Using this free service, authors can make their results available to the community, in citable form, before we publish the edited article. We will replace this *Accepted Manuscript* with the edited and formatted *Advance Article* as soon as it is available.

You can find more information about *Accepted Manuscripts* in the Information for Authors.

Please note that technical editing may introduce minor changes to the text and/or graphics, which may alter content. The journal's standard Terms & Conditions and the Ethical guidelines still apply. In no event shall the Royal Society of Chemistry be held responsible for any errors or omissions in this *Accepted Manuscript* or any consequences arising from the use of any information it contains.

ROYAL SOCIETY OF CHEMISTRY

www.rsc.org/jaas

Journal of Analytical Atomic Spectrometry RSCPublishing

ARTICLE

A large area full-field EDXRF imaging system based on a THCOBRA gaseous detector

Cite this: DOI: 10.1039/x0xx00000x

Received 00th January 2012,
Accepted 00th January 2012

DOI: 10.1039/x0xx00000x

www.rsc.org/

A.L.M Silva,[a] M. L. Carvalho,[b] K. Janssens,[c] and J.F.A. Veloso[a]

By taking advantage of the attractive features in terms of gain, position and energy resolution of the 2D-THCOBRA detector, a new large area Full-Field X-ray Fluorescence Imaging (FF-XRFI) system for EDXRF imaging applications was developed. The proposed FF-XRFI system has an active area of 10x10 cm² and can be used to examine macroscopic samples with a moderately good energy resolution (< 1.6 keV FWHM at 8 keV) and a suitable spatial resolution (~ 500 um FWHM). This combination of characteristics allows to record elemental distribution maps from the surface of different sample types by combining image and energy information. Two different approaches were used for the X-ray optics, one based on a single pinhole and another based on a parallel multiple-hole collimator. To illustrate the system capabilities, some sample examples were imaged and studied.

Introduction

Among the instrumental analytical methods, Energy Dispersive X-ray Fluorescence (EDXRF) analysis is a well-established method, which has grown over the recent years through new developments and applications.

EDXRF analysis is an analytical technique that allows for the determination of multiple elements present in a given sample. In addition, the analysis is in principle non-destructive and can be performed with high precision and accuracy (~few ppm), requires short irradiation time (typically a few minutes) while the associated costs are low when compared to other techniques [1].

Due to the developments in the field of X-ray optics and detector technology, X-ray fluorescence technique evolved from the conventional bulk elemental analysis method to an elemental imaging method with a spatial resolution suitable to study many problems. The energy resolved X-ray Imaging technique allows us to obtain distribution patterns of the chemical elements in multi-component samples, for instance, in biologic samples or cultural heritage materials. It is widely used for environmental, industrial, biological, bio-medicine and scientific research applications [1–6].

This kind of imaging system is usually based on scanning systems in which an X-ray micro-beam scans the sample in both X and Y directions. At each irradiated point, the characteristic photons are collected by using an energy dispersive detector, providing the elemental composition of each scanned point [7–10]. Other alternative is to use a broader X-ray beam to irradiate the entire area of the sample to be imaged and record the fluorescence photons by using a two dimensional energy dispersive detector, without scanning measurements. These systems are known as full-field of view systems and are usually based on pixel detectors, such as Charge Coupled Devices (CCDs) [11,12], Medipix [13] or PILATUS detectors [14].

Most of the scanning systems show both a good position and energy resolution, although they usually need sample preparation and have some limitations regarding sample size, in addition to the limitations inherent to the scanning complexity; they are usually also time consuming. On the other hand, systems based on pixel-detectors mostly have a good position and fair energy resolution although some limitations are inherently present in the detectors themselves while the complexity of the system for imaging readout can also be a limiting factor.

In an attempt to overcome the constraints in terms of portability and cost of the other systems, recently a full-field of view EDXRFI system was introduced based on (a) a 2D gaseous detector with an active area of 2.8×2.8 cm^2, called 2D-Micro-Hole and Strip Plate (2D-MHSP) and (b) a pinhole; this system was mainly employed for cultural heritage [15,16]and biomedical studies [17]. Another EDXRFI system based on a 10×10 cm^2 triple GEM detector combined with pinhole optics was recently introduced [18]. The system was successfully employed for elemental mapping studies related with pigment distributions in fine art paintings. Although both the 2D-MHSP and triple-GEM detectors have shown good results in the field, large area devices are more complex and difficult to produce,

leading to higher costs, when compared with the THCOBRA detector that is described in this work.

The need to perform large area analysis at a relatively low cost has led to the development of a new FF-XRFI system based on a 10×10 cm^2 position sensitive gaseous detector called 2D-THCOBRA [4]. The THCOBRA concept is similar to that of the MHSP, except that it is much more robust, simple and easy to produce for large area devices. It can also be produced in large quantities since it is based on standard printed circuit board technology, making it very cost effective. THCOBRA structures with 30×30 cm^2 were already produced and tested[19].

Below, the performance of the system in terms of energy and position resolution is presented; two different X-ray optical configurations, in which the THCOBRA detector combined with either a single imaging pinhole or with a multi-hole imaging plate are discussed. A number of samples applications are described to illustrate in a concrete manner the capabilities of the system.

Experimental Setup

2D-THCOBRA detector The main component of the system is the X-ray imaging detector, which is based on a Micropattern Gaseous Detector (THCOBRA detector). By implementing a very simple readout system based on resistive lines, the 2D-THCOBRA, a position sensitive detector with an intrinsic imaging capability was developed [4]. Together with the accurate determination of the interaction position of each X-ray photon in the sensitive area of the detector, it carries also the information about the energy of the incoming radiation [4]. It is produced using similar methods as the THGEM (thick gas electron multiplier)[20] by using printed circuit board technology and by drilling holes through the board.

The 2D-THCOBRA uses an active area of 10×10 cm^2. It is a double-sided structure made out of a 0.4 mm thick G10 fiberglass-epoxy laminate plate, covered with a 50 µm thick layer of copper on both sides. On the bottom side, a pattern of strips is etched: a circular electrode is surrounding each hole having a 0.2 mm width (cathode). The adjacent anode strips are also 0.2 mm wide (Figure 1). In order to provide the 2D detection capability, the strips on the top side are orthogonally oriented relative to the anode strips, thus exhibiting a zigzag-shape that circumvents the holes in the plate.

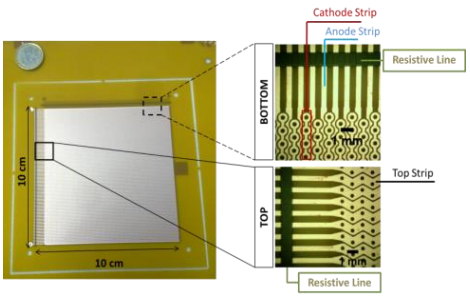

Figure 1 Photo of a 10x10 cm^2 position sensitive THCOBRA. Detailed view of the top and bottom side of the micro-hole structure [4].

The detector employs a continuous flow of a Ne/5%CH4 gas mixture, allowing to continuously refreshing the gas inside the detector chamber. Figure 2b-c show the 2D-THCOBRA based detector when used during the experiments performed in this work. The detector system consists of an aluminium vessel containing (a) a metallic mesh to define the drift region, (b) a THGEM and (c) a THCOBRA plate arranged in a cascade configuration. The 10×10 cm^2 THGEM employed here plays the role of a preamplification stage [4].

Figure 2c shows the operation principle of the 2D-THCOBRA detector. The filling gas acts as the absorption and multiplication medium. The first charge multiplication events occur due to the intense electric field inside the holes, produced by the voltage difference applied between the cathode and the top strips, at a potential VCT. By controlling the voltage difference between the circular-cathode strips and the anodes (at VAC), a second multiplication stage can occur. The charge is collected at the anode strips [4].

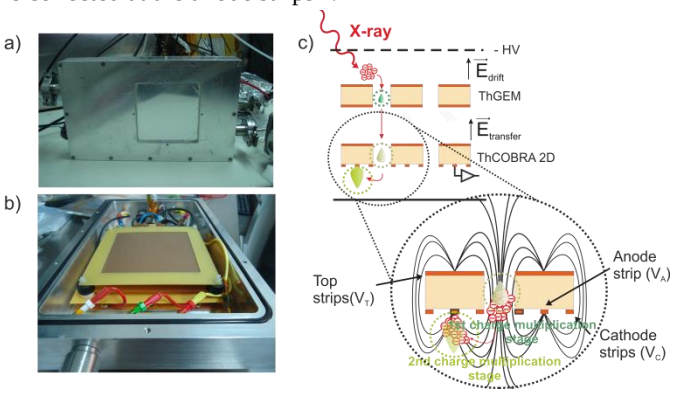

Figure 2 2D-THCOBRA detector used in the experiments performed during this work. a) Photo of the detector; b) Inside view of the detector: the THGEM and the THCOBRA are disposed in a cascade configuration; and c) Operation principle of the detector [4].

Two thin orthogonal resistive lines (~1.2 kΩ/cm), simple to apply by serigraphy methods, connect the top strips (top side) and the anode strips (bottom side) and allow to obtain information on both the X- and Y- positions where the X-ray photons impinged on the detector (see Figure 3). The anode and top signal is collected from both ends of each resistive layer, according to the principle of resistive charge division [4].

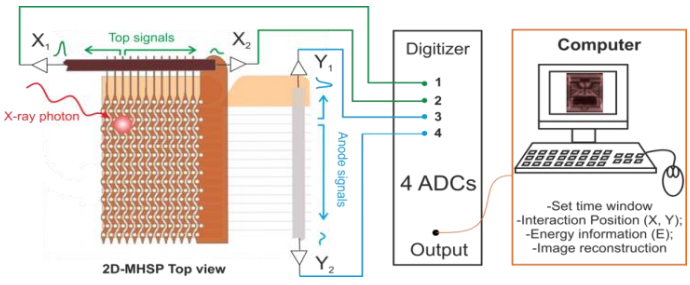

Figure 3 Schematic of the operation principle of the THCOBRA detector for 2D-imaging.

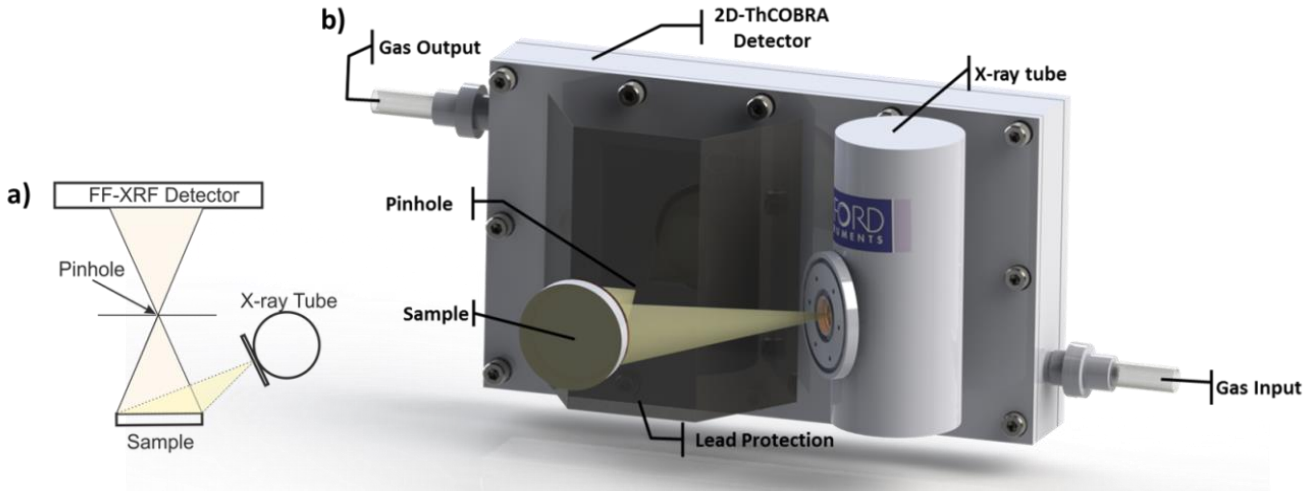

Figure 4 a) Schematic of the basic components of a FF-XRF imaging system, using a pinhole camera as X-ray imaging device, as well as their geometric arrangement; b) Experimental setup based on the 2D-THCOBRA detector.

Thus, through the ratio between these charge amplitudes is it possible to determine the center of the electron avalanche distribution in the Cartesian coordinate system:

$$X = k\frac{X_1}{X_1 + X_2}$$

$$Y = k\frac{Y_1}{Y_1 + Y_2}$$

where X1 and X2 are the amplitudes of the charge signals collected in the X direction, Y1 and Y2 are the amplitudes of the charge signals collected in the Y direction, and k represents a calibration factor. X and Y are the measured positions of the interaction of X-rays within the 2D-THCOBRA detector. The energy information can also be obtained by summing both signals from one resistive line, which represents the total produced charge by the incoming X-ray.

EDXRF imaging system The EDXRF imaging system based on the 2D-THCOBRA detector is composed of an X-ray tube, a lead pinhole, and the 2D-THCOBRA detector. These components are arranged in an appropriate and well-defined geometry when performing the measurements, as shown in Figure 4.

The X-ray tube irradiates the sample with an angle of about 45°. The pinhole is incorporated in a 1.5 mm thick lead foil to avoid the detection of scattered photons that do not pass via the pinhole optics onto the detector.

The pinholes of 0.5, 1, 1.6 and 2 mm diameter used during this work were produced by drilling appropriate holes in 300 µm thick lead foils. Their transmission for photon energies up to 30 keV is negligible. Replacement of the pinholes between acquisitions was always carried out with great care and without changes in the geometry of the system.

The position of the pinholes was determined in order to establish the adequate magnification for each acquisition $\left(M = \frac{detector-pinhole\ distance}{sample-pinhole\ distance}\right)$. On the other hand pinhole cameras were always kept as close as possible to the detector in order to get the best detection efficiency conditions.

Energy Resolution and Linearity

The energy resolution offered by the 2D-THCOBRA detector can be inferred from its response to mono-energetic X-ray sources.

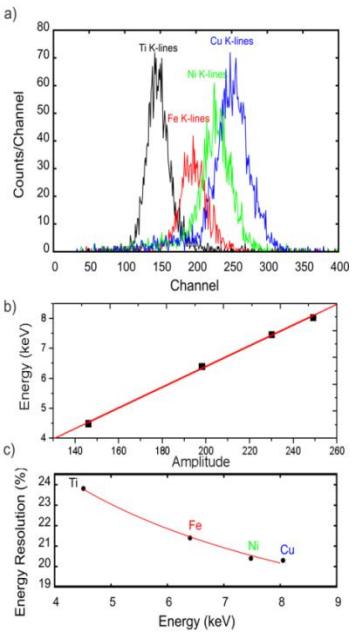

Figure 5 a) Fluorescence radiation spectra of different element targets: Ti, Fe, Ni and Cu; b) pulse amplitude and c) energy resolution are plotted against detected photon energy.

In this case, the fluorescence X-ray lines from different single-element targets such as Ti, Fe, Ni and Cu were employed.

The single-element targets were placed 20 cm away from the detector window and excited through irradiation with the X-ray tube. The current and the voltage on the X-ray tube were set in accordance to the analyzed target. A lead collimator with a 4 mm diameter hole was placed in front of the detector window.

Some of the obtained spectra are shown in Figure 5a. A good linearity, with a deviation of about 9.3×10^{-4} keV/Channel, was achieved for the measured amplitude as a function of the X-ray energy, as shown in Figure 5b. The relative energy resolution was determined by fitting a Gaussian distribution to the peak of the fluorescence K-lines, and was found to be $\Delta E/E$ = 23.8%, 21.4%, 20.4% and 20.3%, for Ti, Fe, Ni and Cu respectively, as shown in Figure 5c. As expected, the points follow an $E^{-1/2}$ dependency [4]:

$$\Delta E/E = (3.1 \pm 0.2) \times 10E^{-1/2} + (9.3 \pm 0.7)$$

Optical System and Spatial Resolution

Pinhole Camera When designing a system for imaging X-ray emitters, a major consideration is which device to use to form an image of the incoming photons on the detector. The pinhole camera is simply a (small) aperture through which the fluorescence photons must pass in order to be recorded by the detector. This device provides a cone-beam image incident into the detector with the focus point at the pinhole. This type of 'optic' combines easy manufacture with the possibility of image magnification; overcomes the spatial resolution limits imposed by the intrinsic detector response, as previously demonstrated [15].

To yield an optimal spatial resolution of the imaging system, the pinhole aperture needs to be as small as possible. However, reducing the pinhole diameter to improve imaging resolution will produce a quadratic reduction of the pinhole camera efficiency [15]. The relative sensitivity of the pinhole collimator was measured by considering the number of photons that pass through the aperture of the collimator reaching the detector relative to the number of photons reaching the detector for the case of the 500 µm-diameter pinhole (relative sensitivity = 1) (Figure 6). The material used in these experiments (Figure 7) was a phantom sample (A) with known composition/structure, composed of five different elements: Ti, Fe, Cu, Ge and Zr.

On the other side, to evaluate in a qualitative way the influence of the pinhole diameter on the obtained spatial resolution, a simple experimental study was performed using the EDXRF imaging 2D-THCOBRA based system.

The pinhole-to-detector and object-to-detector distance were set to equal values, in this case, in order to obtain images without magnification, and were kept constant for all the acquisitions. The acquisitions were performed with the X-ray tube operating at 20 kV and 1 mA. The acquisition time was 15 min.

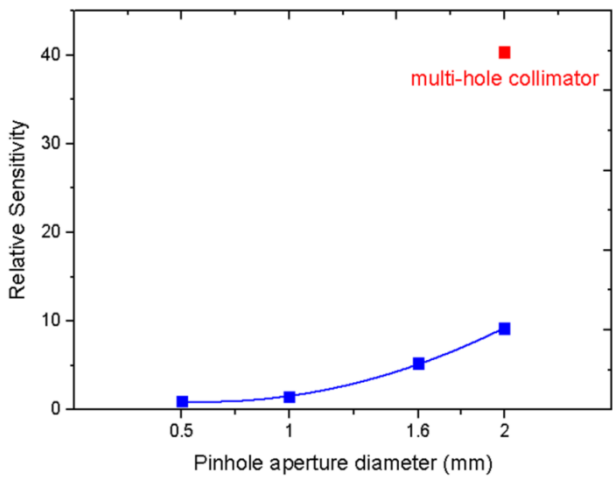

Figure 6 Relative sensitivity of the pinhole as a function of its aperture diameter.

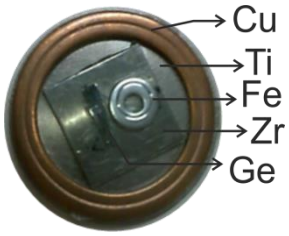

Figure 7 Photo of multi-element phantom sample A, composed of Ti, Fe, Cu, Ge and Zr.

A summary of the obtained spectral distributions and corresponding images is presented in Figure 8.

By using a dedicated software for image acquisition, processing and visualization of the results, it is possible to choose a Region-Of-Interest (ROI) in the spectrum (energy dimension) and plot the corresponding distribution of the photons with energies falling within this ROI. In this manner, X-ray photons corresponding to a characteristic line can be selected, yielding the map of a specific element. 3 elemental maps may further be combined into a RGB composite image by attributing a different primary color (red, blue, green) to each ROI map. We can also access the information about the intensity distribution in the elemental images which can be useful, for instance, to later infer about the relative quantities of each element in the sample. In Figure 8, by selecting different energy ROIs, it is possible to identify the different elements that make up the sample: Ti, Fe and Cu+Ge. Due to limitations of our software (that only allows 3 maps to be selected simultaneously), for the latter two elements, only one ROI was used. Note that the Zr plate can only be observed by the absence of X-rays, due to the fairly low X-ray tube voltage that was employed (20 kV) and the low detection efficiency of the detector medium (Ne/5%CH4) for the characteristic K lines of Zr (15.77 keV).

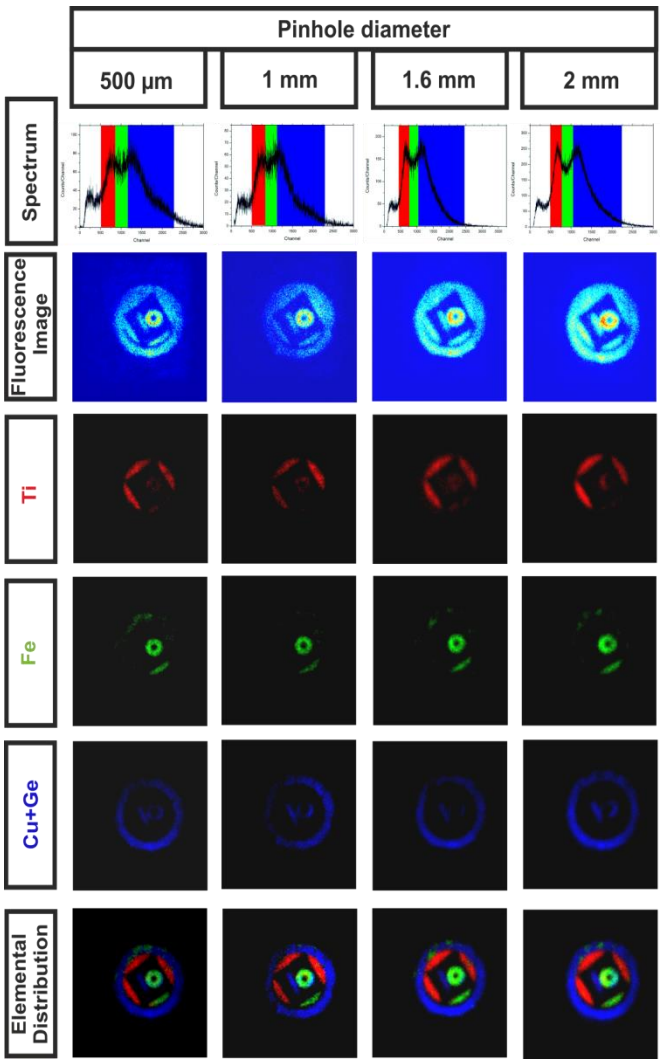

Figure 8 Image results obtained from phantom sample A by employing lead pinholes with different diameters as image defining element.

Qualitatively speaking, Figure 8 shows that the spatial resolution and image quality offered by the imaging system is better for pinholes with smaller apertures, as was demonstrated in ref.[21]. However, it is evident that for larger apertures, the number of photons detected per second is much higher, leading to a higher efficiency (Figure 6), which in results in images composed of (much) more detection events for the same acquisition time. It can be concluded that the optimal pinhole apertures to be used will depend on the specific application and that often a compromise choice will need to be made. When the photon flux is high (due to elevated concentrations of some elements) it becomes possible to use smaller pinhole apertures, favouring the position resolution; on the other side, when the emitted X-ray flux is low, the use of a pinhole with larger diameter is more appropriate in cases where a lower level of spatial resolution is not critical (e.g. for samples with limited heterogeneity).

System Spatial Resolution To evaluate the spatial resolution of the 2D-THCOBRA-based system in a quantitative manner, images were recorded from a sample composed of a stainless steel gasket and a rectangular piece of Ge, placed on a Perspex support (phantom sample B).

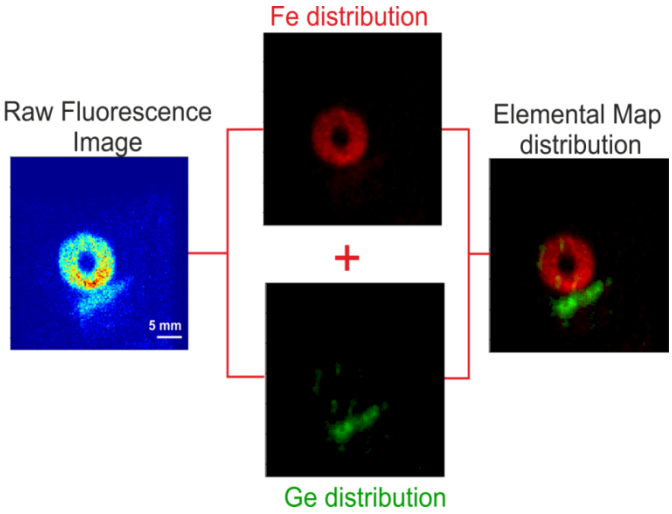

Figure 9 Raw X-ray fluorescence image (left) individual elemental images corresponding to the Fe and Ge distributions (center) and RG composite map obtained from phantom sample B. A pinhole magnification geometry of 3 was used.

A pinhole of about 500 µm diameter was employed and the pinhole-to-detector and sample-to-pinhole distances were adjusted in order to realize a magnification of about 3. An X-ray tube voltage of 22 kV and an anode current of 1 mA were used in this case.

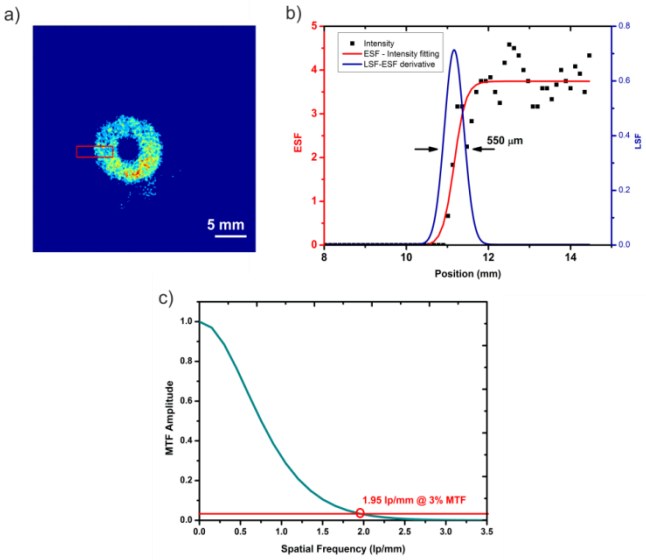

Figure 10 a) Fluorescence image of phantom sample B obtained using a magnification of x3. The selected region for spatial resolution calculations is indicated by the red rectangle. b) ESF and LSF used to determine the position resolution of the image in a); c) MTF corresponding the LSF shown in b).

The results are shown in Figure 9. In the spectral distributions, both elements present can be easily identified while the maps correctly reflect their lateral distribution. Typically, during XRF experiments, higher tube voltages than 20-25 keV are employed in order to excite as many elements as possible during one measurement. In the present case, however,

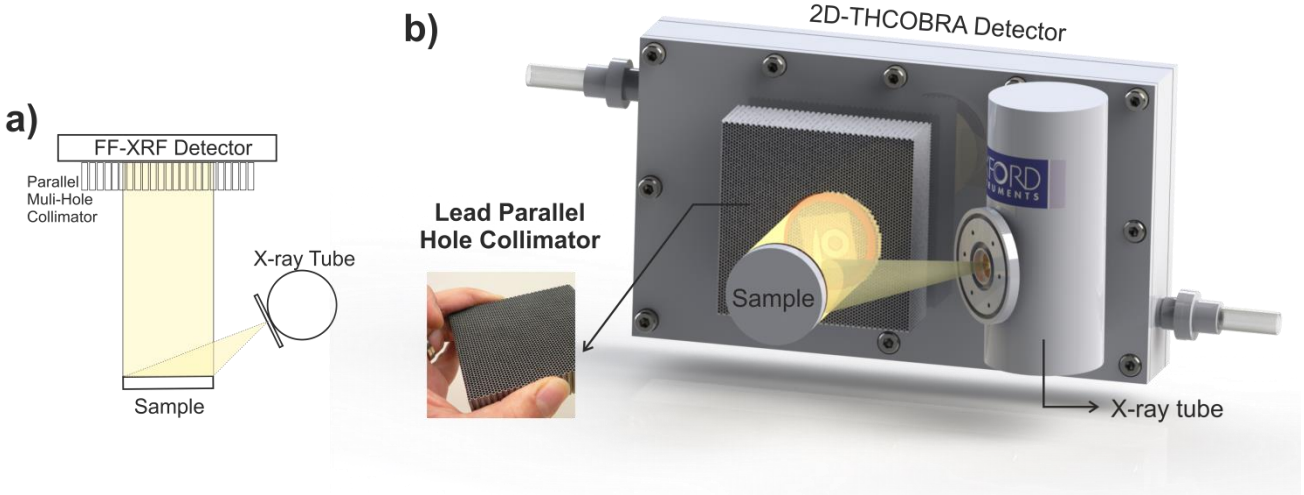

Figure 11 a) Top-down view schematic of a EDXRF imaging system using a parallel multi-hole collimator; b) EDXRF imaging system based on the 2D-THCOBRA detector and a multi-hole collimator plate as imaging optic

we have employed a relative low voltage in order to excite more efficiently the elements that were known to be present and in order to reduce the background.

The spatial resolution of the system was evaluated by employing the Fe-image and using Edge Spread Function (ESF)[22] method. Figure 10 shows the image of the Fe spatial distribution and the correspondent ESF, the Line Spread Function (LSF) and Modulation Transfer Function (MTF). As can be seen, a LSF FWHM of about 550 µm was obtained together with a resolution of 1.95 lp/mm (line-pairs/millimetre) at a MTF amplitude of 3%. This means that for X-ray photon energies near 6 keV spatial features above 550 µm can be well resolved.

The spatial resolution of the imaging system is determined by the intrinsic position resolution of the detector augmented with the contribution of the imaging pinhole[15]. In the present case and for the relatively low energy range (Fe- to Ge-Kα, or 6.3-9.8 keV) used, the major contribution to the spatial resolution is by the pinhole. This depends mostly on its diameter but also on the magnification geometry employed during the acquisition. At higher energies, the intrinsic position resolution of the detector is expected to be the dominating contribution to the overall spatial resolution of the system. A recent study has shown that especially for energies above 15 keV, the photoelectron range in Ne/5%CH4 limits the intrinsic position resolution of a gaseous detector. This study has shown also that gases as Kr and Xe are the recommended filling gases to overcome this limitation [23].

Multi-hole collimator Another approach that may be employed to increase the total photon flux reaching the imaging system involves the use of a parallel multi-hole collimator. For demonstration of this approach, we have used a lead collimator, widely used in medical systems such as gamma cameras. In this way, only the characteristics X-rays photons emitted from the sample in the direction orthogonal to the detector window can go through the collimator holes and be detected. This results in a projection image of the sample produced by the characteristics X-rays.

By using a 10x10 cm^2 parallel multi-hole collimator with 2 mm hole size (200 µm septa and 4 cm length), a fluorescence image of phantom sample A was again acquired. The multi-hole collimator plate was coupled to the detector window, as shown in Figure 11, in order to increase the collimator efficiency and also to obtain the better position resolution possible. The experimentally determined relative sensitivity of this system is indicated in Fig. 6; it is 4-40 times higher than in the case of the 2 and 0.5 mm diameter pinholes, respectively.

Some of the images recorded from phantom sample A are shown in Figure 12. Despite the higher sensitivity, there are some disadvantages associated with the use of the multi-hole approach: the collimator plate always projects an image of the same size as the object onto the detector, contrary to the single pinhole that allows obtaining images of the objects with different magnifications depending on the geometry employed.

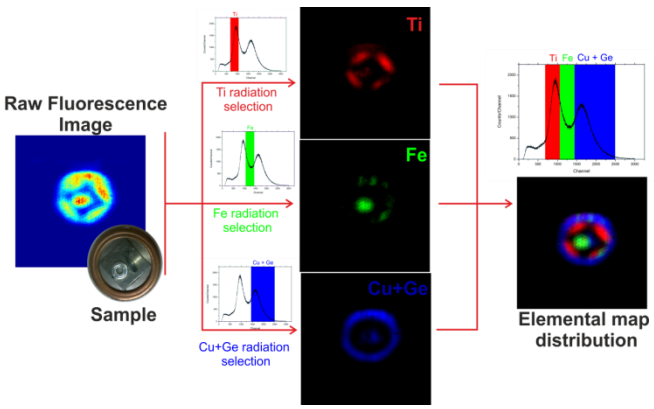

Figure 12 Element specific images obtained from phantom sample A using the multi-hole plate as imaging forming optic. (left) raw X-ray fluorescence image; (middle) individual elemental images (Ti, Fe, Cu+Ge); (right) composite RGB map.

This can be a problem when it is of interest to image a small region of the sample in great detail. Also, the higher complexity and cost of the multi-hole collimator needs to the taken into account. The lower spatial resolution that is obtained with the multi-hole plate is mainly due to the larger inner diameter of the holes (2 mm). In the resulting XRF images, also the shape of the collimator holes is visible.

We can conclude that this type of collimator plate could be an interesting solution for some imaging applications; however, the hole size should to be much smaller (e.g. < 0.5 mm) in order to reach the ultimate spatial resolution of the system (i.e., close to the intrinsic position resolution of the detector).

System demonstration: XRF imaging of an Illuminated parchment

XRF is one of the most popular diagnostic techniques for the conservation of works of art since it is a well-established technique for elemental analysis. It can identify many elements in an efficient way, depending on the system used and is non-destructive in nature[1,24].

By using the EDXRF imaging system based on the 2D-THCOBRA device, fluorescence images were acquired of a single folio from an illuminated 15th-16th century Book of Tides. The folio examined is shown in Figure 13 and Figure 14. An illuminated manuscript is a document which includes ornamental borders, illustrations, and other decoration motifs besides the text itself. The term *manuscript* typically refers to any document produced manually, through handwriting, whereas the illumination term refers to the frequent incorporation of gold or sometimes silver onto the manuscript.

The brilliant colors based on these elements often give the impression that the manuscript is emitting light, i.e., is illuminated [1]. Often, the aim of studies involving the identification of the pigments employed in a particular manuscript is to identify the method used by the artist during the elaboration of the document. Sometimes the indirect estimation of the approximate age of the artifact is attempted via pigment analysis. This information is often useful during restoration, cleaning and conservation processes[1]. Occasionally, different 'hands' can be distinguished from each other in the case of manuscripts that were produced by different artists using (slightly) different materials.

The text is written in black color. Some red/pink marks and lines that appeared to have served as writing alignment rulers are visible along the manuscript. On the right margin of the front side and on the left margin of the back side of the parchment folio a vertical band of illuminations are present. Some rural/pastoral motives, such as strawberries and floral motifs inside gilded circles are present as well as some scroll works drawn in blue and gilded ink/paint.

Elemental data were recorded with the system of Figure 4 while irradiating the folio with primary X-rays generated by a low power Oxford Instruments Mo-tube. Prior to these measurements, some studies were already performed using μ-Raman spectroscopy, μ-XRF and μ-X-ray diffraction [24]. The conclusions from these studies facilitate the interpretation of the obtained results.

The first images obtained with the experimental setup of Figure 4 are depicted in Figure 13 and were acquired with a

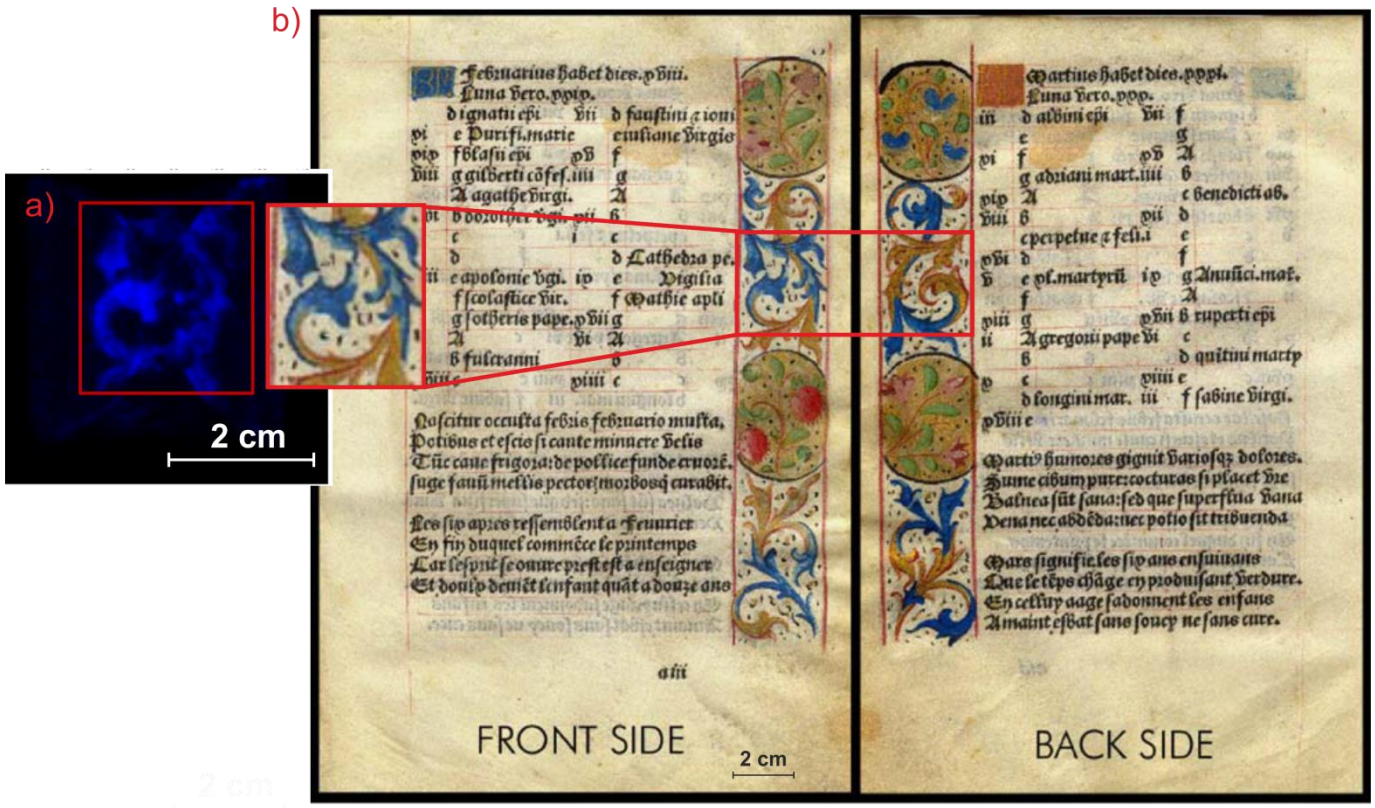

Figure 14 a) Acquired image with a detail of the parchment irradiated area. b) Photo of the front and back side of the illuminated parchment, showing that to a gilded area on the front side, has a corresponding blue painted area on the reverse side.

magnification factor of about x2.5. The acquisition was performed with the X-ray tube operating at 25 kV and 1 mA, and the acquisition time was of about 15 min. The spectrum (Figure 13b) shows an important Ca peak, which can be attributed to the chalk used during the preparation of the parchment [24]. By selecting in the spectrum a ROI corresponding to the characteristic energy range of Ca, we can obtain an image of its spatial distribution in the irradiated area of the parchment (Figure 13c). As can be seen, this element is almost uniformly distributed within the irradiated area; only a slightly increase in intensity is observed in the painted area. This is because chalk ($CaCO_3$) was often used as filler in paint, as mentioned in ref. [24].

By selecting in the spectrum another ROI corresponding to the second peak in the spectrum (Figure 13b), an image showing part of the scroll work is obtained (Figure 13d).

If we look carefully at the painted picture, we can see that the region of the acantus leaves, painted with blue paint, appears to be more intense that the gilded region.

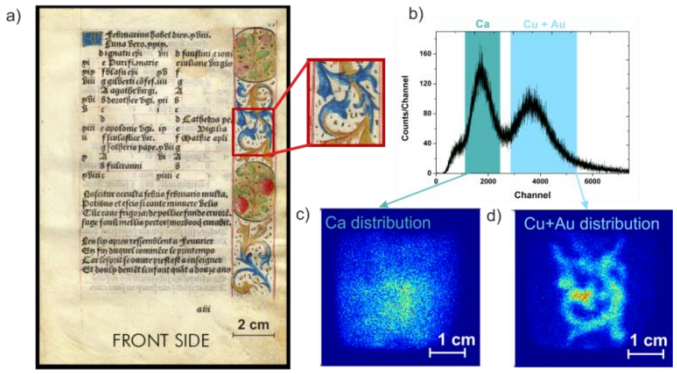

Figure 13 a) Photograph of the front side of the illuminated parchment, including a detailed view of the analyzed region; b) total pulse-height spectrum with different ROIs selected , corresponding to the elements Ca and Cu+Au; c) Ca and d) Cu+Au maps.

According to ref. [24], the blue pigment employed here is azurite, a basic copper(II) carbonate, one of the important blue pigments in European painting until the eighteenth century. Concerning the gilded region, we should expect to see in the spectrum the L-lines of Au. However, in that case it was not possible to distinguish the characteristic K-lines of Cu (8 keV) from the characteristic L-lines of Au (10 keV), mainly due to the limited energy resolution of the detector at that time. The difference in the Cu/Au intensities observed in the image are caused by the fact that in the case of Au we are detecting the L-lines, which per unit of irradiated mass, are much less intense than the K-lines of Cu.

Figure 14 shows the XRF image obtained with the 2D-THCOBRA-based EDXRF imaging system when employing a high power X-ray tube. This tube was operating at 30 kV and 40 mA and was placed about 30 cm away from the sample. The XRF image was acquired with a magnification of about x2.7 and corresponds to the same analyzed region as before (Figure 14a). Also in this case, it was not possible to completely separate the distribution of Cu from that of Au. Next to limitations in detector resolution that does not allow for a complete separation of the signals of these two elements in the energy dimension, also the fact that in the areas that have blue paint of the front side, gold paint is present on the back side (and vice versa), causes the signals of Au and Cu to overlap in the spatial dimensions. Macroscopic XRF scans of this area (see ref. [25] for details on the instrumentation employed), in which the Cu and Au contributions are well separated in the energy dimension, show similar distributions (Figure 15). This is due to the penetration depth of the X-rays through the parchment sheet, which can lead to some interpretation problems. It should be noted that while the Au-L and Cu-K MA-XRF maps of Figure 15 present a much better spatial resolution (due to the use of a scanning step of 50 µm), the acquisition time required was almost 100 times higher than for the 2D-THCOBRA-based system.

The maps of Fig. 13 and 14 show almost the same information as those of Fig. 15 and feature a reasonable spatial resolution.

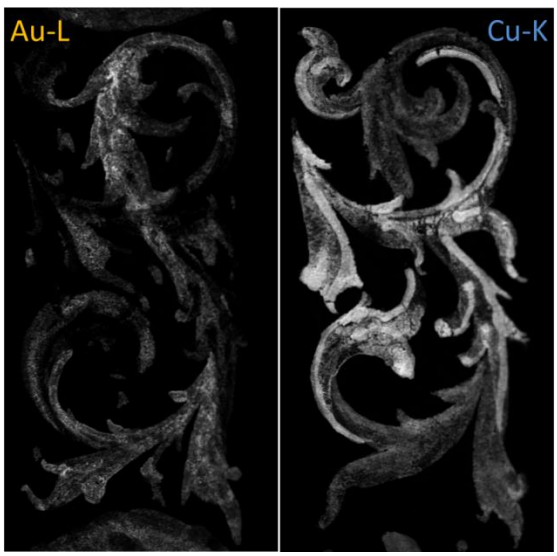

Figure 15 Macro-XRF scanner[24] map from the acantus leaves of the parchment. Acquisition conditions: XOS XBeam tube with PC lens; 50 µm steps; 0.2 s/pixel; 24h total scanning time. Image size: 447x886 pixels.

Conclusions and Future work

In this work, an EDXRF imaging system based a 2D-THCOBRA detector was developed and its capabilities for element specific imaging examined. By taking advantage of the photon counting capability of this detector, which allows both position and energy response of series of X-ray photons to be stored in parallel, elemental maps of large samples can be recorded.

The diameter of the pinhole used has a strong influence on the photon flux reaching the detector and also on the obtained spatial resolution of the system. A system spatial resolution of about 500 µm was achieved for a 1 mm aperture pinhole diameter.

The detector has shown a relative energy resolution of about 22% for 6.4 keV X-ray photons.

The results obtained from the first implementation of the system using phantom samples with known structure/composition have demonstrated it applicability, since it enabled the identification of the different elements present and could visualize their spatial distribution in the irradiated sample.

After the validation of the system, a more complex sample was analysed: an illuminated parchment from the 15th-16th century.

By using the XRF image obtained using the 2D-THCOBRA based system, it was possible to identify the presence of Ca, corresponding to the parchment and the Cu K- and Au L-line intensity distribution.

The major advantage of the proposed system is the high sensitive area (which can be produced in sizes larger than 30×30 cm^2) and the low cost of the detectors. The cost associated with its production is around 3€/cm^2, which makes it tremendously competitive against most of the other types of energy dispersive detectors, even when the additional cost of the readout electronics is taken into account. The latter cost can be further decreased in the case of large scale industrial production. Thus, even when compared to systems with a better energy resolution, the proposed detector systems are considered competitive, offering a considerably larger detection area at a significantly lower price.

Optimization of the energy resolution and detection efficiency of the detector is crucial for the proposed applications; for this reason, future work will focus on the improvement of the gas detection medium. Replacing Ne with heavier noble gases such as Xe or Kr, will significantly improve the intrinsic energy resolution. Since this also leads to a lower photoelectron range, the intrinsic position resolution will improve, making it more suitable for EDXRF imaging applications.

Finally, to increase its portability, the packaging of the 2D-THCOBRA detector will be modified to that it can be used as a sealed detector.

Acknowledgements

The authors thank Stijn Legrand for acquisition of the MAXRF maps shown in Fig. 15. This work was partially supported by projects CERN/FP/123604/2011 FEDER, COMPETE and FCT (Lisbon) programs. A.L.M. Silva is supported by QREN programme Mais Centro – Programa Operacional Regional do Centro, FEDER and COMPETE, through project Biomaterials for Regenerative Medicine (CENTRO-07-ST24-FEDER-002030).

Notes and references

[a] I3N-Physics Department of University of Aveiro, 3810-193 Aveiro, Portugal

[b] Atomic Physics Centre, University of Lisbon, 1649-003 Lisboa, Portugal

[c] AXES Research group, Department of Chemistry, University of Antwerp, Groenenborgerlaan 171, 2020 Antwerp, Belgium

1. S. Pessanha, M. Manso, and M. L. Carvalho, *Spectrochim. Acta Part B At. Spectrosc.*, 2012, **71-72**, 54–61.
2. J. Uher, G. Harvey, and J. Jakubek, *IEEE Trans. Nucl. Sci.*, 2012, **59**, 54–61.
3. J. F. C. A. Veloso, A. L. M. Silva, C. A. B. Oliveira, A. L. Gouvêa, C. D. R. Azevedo, L. Carramate, H. Natal da Luz, and J. M. F. dos Santos, *Spectrochim. Acta Part B At. Spectrosc.*, 2010, **65**, 241–247.
4. A. L. M. Silva, C. D. R. Azevedo, L. F. N. D. Carramate, T. Lopes, I. F. Castro, R. de Oliveira, and J. F. C. A. Veloso, *J. Instrum.*, 2013, **8**, P05016–P05016.
5. J. Žemlička, J. Jakůbek, M. Kroupa, and V. Tichý, *Nucl. Instruments Methods Phys. Res. Sect. A Accel. Spectrometers, Detect. Assoc. Equip.*, 2009, **607**, 202–204.
6. B. Norlin, C. Fröjdh, E. Fröjdh, M. O. Nils, A. Fröjdh, and G. Thungström, in *2009 IEEE Nuclear Science Simposium Conference Record*, 2009, pp. 1703–1706.
7. U. Bergmann, P. L. Manning, and R. A. Wogelius, *Annu. Rev. Anal. Chem. (Palo Alto. Calif).*, 2012, **5**, 361–89.
8. R. G. Figueroa, E. Lozano, F. Belmar, D. Alcaman, A. von Bohlen, C. A. B. Oliveira, A. L. M. Silva, and J. F. C. A. . Veloso, *X-Ray Spectrom.*, 2014, **43**, 126–130.
9. R. Alberti, C. Fiorini, C. Guazzoni, T. Klatka, and a. Longoni, *Nucl. Instruments Methods Phys. Res. Sect. A Accel. Spectrometers, Detect. Assoc. Equip.*, 2007, **580**, 1004–1007.
10. G. Vittiglio, S. Bichlmeier, P. Klinger, J. Heckel, W. Fuzhong, L. Vincze, K. Janssens, P. Engström, a. Rindby, K. Dietrich, D. Jembrih-Simbürger, M. Schreiner, D. Denis, a. Lakdar, and a. Lamotte, *Nucl. Instruments Methods Phys. Res. Sect. B Beam Interact. with Mater. Atoms*, 2004, **213**, 693–698.
11. M. Alfeld, K. Janssens, A. Sasov, X. Liu, A. Kostenko, K. Rickers-Appel, G. Falkenberg, M. Denecke, and C. T. Walker, in *CP1221, X-ray Optics and Microanalysis. Proceedings of the 20th International Congress*, 2010, vol. 111, pp. 111–118.
12. M. G. Vasin, Y. V. Ignatiev, a. E. Lakhtikov, a. P. Morovov, and V. V. Nazarov, *Spectrochim. Acta Part B At. Spectrosc.*, 2007, **62**, 648–653.
13. V. Tichy, T. Holy, J. Jakubek, V. Linhart, S. Pospisil, and Z. Vykydal, *Nucl. Instruments Methods Phys. Res. Sect. A Accel. Spectrometers, Detect. Assoc. Equip.*, 2008, **591**, 67–70.
14. P. Kraft, a Bergamaschi, C. Broennimann, R. Dinapoli, E. F. Eikenberry, B. Henrich, I. Johnson, a Mozzanica, C. M. Schlepütz, P. R. Willmott, and B. Schmitt, *J. Synchrotron Radiat.*, 2009, **16**, 368–75.
15. A. L. M. Silva, C. D. R. Azevedo, C. A. B. Oliveira, J. M. F. Dos Santos, M. L. Carvalho, and J. F. C. A. Veloso, *Spectrochim. Acta Part B At. Spectrosc.*, 2011, **66**, 308–313.

16. A. L. M. Silva, C. A. B. Oliveira, A. L. Gouvêa, J. M. F. dos Santos, M. L. Carvalho, and J. F. C. A. Veloso, *Anal. Bioanal. Chem.*, 2009, **395**, 2073–80.

17. A. L. M. Silva, R. Figueroa, A. Jaramillo, M. L. Carvalho, and J. F. C. A. Veloso, *Spectrochim. Acta Part B At. Spectrosc.*, 2013, **86**, 115–122.

18. A. Zielińska, W. Dąbrowski, T. Fiutowski, B. Mindur, P. Wiącek, and P. Wróbel, *J. Instrum.*, 2013, **8**, P10011.

19. M. Alexeev, R. Birsa, F. Bradamante, A. Bressan, M. Büchele, M. Chiosso, P. Ciliberti, S. D. Torre, S. Dasgupta, O. Denisov, V. Duic, M. Finger, M. F. Jr, H. Fischer, M. Giorgi, B. Gobbo, M. Gregori, F. Herrmann, and J. F. C. A. Veloso, *J. Instrum.*, 2014, **9**, C03046.

20. R. Chechik, *http:///ftp/arxiv/papers/0712/0712.0485.pdf*.

21. R. Accorsi and S. D. Metzler, *IEEE Trans. Med. Imaging*, 2004, **23**, 750–63.

22. S. W. Smith, *The Scientist and Engineer's Guide to Digital Signal Processing*, California Technical Pub., 1997.

23. C. D. R. Azevedo, S. Biagi, R. Veenhof, A. L. M. Silva, P. M. Correia, and J. F. C. A. Veloso, *Submitt. to Phys. Lett. B*, 2014.

24. G. Van der Snickt, W. De Nolf, B. Vekemans, and K. Janssens, *Appl. Phys. A*, 2008, **92**, 59–68.

25. M. Alfeld, J. V. Pedroso, M. van Eikema Hommes, G. Van der Snickt, G. Tauber, J. Blaas, M. Haschke, K. Erler, J. Dik, and K. Janssens, *J. Anal. At. Spectrom.*, 2013, **28**, 760–767.

